ARTICLES
https://doi.org/10.1038/s41567-019-0517-5
nature physics

Chiral topological superconductivity arising from the interplay of geometric phase and electron correlation

Wei Qin, Leiqiang Li and Zhenyu Zhang *

In modern theory of solids, many-electron correlations can give rise to superconductivity, while the Berry or geometric phase is responsible for non-trivial topology. So far, these two physical ingredients have been taken into account only in a simple additive manner. Here, we carry out a systematic study of the interplay between geometric phase and electron correlation as well as their combined effects on topological and superconducting properties. Based on first-principles studies of Pb_3Bi/Ge(111) as a prototypical system, we develop a generic two-dimensional effective formalism that respects hexagonal symmetry with Rashba spin–orbit coupling, displays a van Hove singularity and includes geometric phase-decorated electron correlations. Our functional renormalization group analysis shows that superconductivity dominates the competing orders in the weak interaction regime, with two consequences. First, the renormalized geometric phase flows to three stable fixed points, favouring chiral ($p_x \pm ip_y$)-wave and *f*-wave superconducting states. Second, the corresponding superconductivity can be substantially enhanced. We construct the phase diagram of the topological quantum states, and identify hole-doped Pb_3Bi/Ge(111) as an appealing platform for realizing chiral topological superconductivity in two-dimensional systems that are highly desirable for detecting and braiding Majorana fermions.

A single-electron state evolving adiabatically in reciprocal space will accumulate a quantum phase known as the Berry or geometric phase[1–3]. Fundamentally, the geometric phase is closely related to topological states of matter, providing a powerful tool in formulating the various quantized topological invariants[2,4–6]. For example, the quantization of Hall conductance in a two-dimensional (2D) Chern insulator[7] can be interpreted as the geometric phase accumulation along a closed loop enclosing the Brillouin zone[2]. Beyond the single-electron picture, the concept of geometric phase has also been generalized to the Cooper pairing state of superconductors, in that the superconducting order parameter can directly inherit its geometric phase from the two paired electrons[8,9]. Depending on the specific phase accumulation of the superconducting order parameter as it winds around the Fermi surface, superconductors can be distinguished into topologically trivial and non-trivial classes[10–15]. Such topological superconductors could harbour non-abelian Majorana fermions[14–17], which can be exploited for fault-tolerant topological quantum computation[18].

So far, two dominant approaches have been suggested to realize topological superconductors. The first is based on the proximity effect, invoking heterostructures of a conventional *s*-wave superconductor with either a topological insulator[19] or a semiconductor with strong Rashba spin–orbit coupling[20]. The second approach is to obtain intrinsic topological superconductors, for example by converting topological insulators or topologically trivial superconductors into topological superconductors using carefully chosen dopants[13,21]. Each of the two proposed approaches has motivated intensive experimental efforts, resulting in the discoveries of several topological superconductor systems[22–28]. However, controversies remain surrounding each system, especially with regard to the observations of Majorana zero modes or fermions. Moreover, in all the existing theoretical treatments of the topological superconductors, the geometric phase that leads to non-trivial topology and electron correlations that are responsible for superconductivity have been taken into account in a simple additive manner. On a more profound fundamental level, it is conceptually intriguing and of paramount importance to investigate how these two essential physical ingredients mutually influence each other in characterizing candidate topological superconductor systems, given the fact that both reflect electron correlations, albeit of different microscopic origins.

In this Article, we carry out a systematic study of the interplay between electron correlation and geometric phase as well as their cooperative effects on topological and superconducting properties. Because the geometric phase vanishes in systems with simultaneous time-reversal symmetry and inversion symmetry[3], we start from a prototypical system consisting of an alloyed monolayer of Pb_3Bi grown on Ge(111), where the inversion symmetry is naturally broken by the substrate. Based on the results of first-principles calculations, we develop a generic 2D effective formalism that respects hexagonal symmetry with Rashba spin–orbit coupling, contains a type II van Hove singularity[29] and exhibits geometric phase-decorated electron correlation[30]. We derive a set of complex renormalization group (RG) flow equations and demonstrate that superconductivity dominates the competing orders in the weak interaction regime. In addition, the interplay between geometric phase and electron correlation results in two constructive consequences. First, the basin of the renormalized geometric phase flows to three stable fixed points, favouring chiral ($p_x \pm ip_y$)-wave and *f*-wave superconducting states. Second, the corresponding superconductivity can be substantially enhanced. We then construct the phase diagram of the topological quantum states, and identify Pb_3Bi doped to the van Hove filling in

International Center for Quantum Design of Functional Materials (ICQD), Hefei National Laboratory for Physical Sciences at the Microscale (HFNL) and Synergetic Innovation Center of Quantum Information and Quantum Physics, University of Science and Technology of China, Hefei, Anhui, China.
*e-mail: zhangzy@ustc.edu.cn

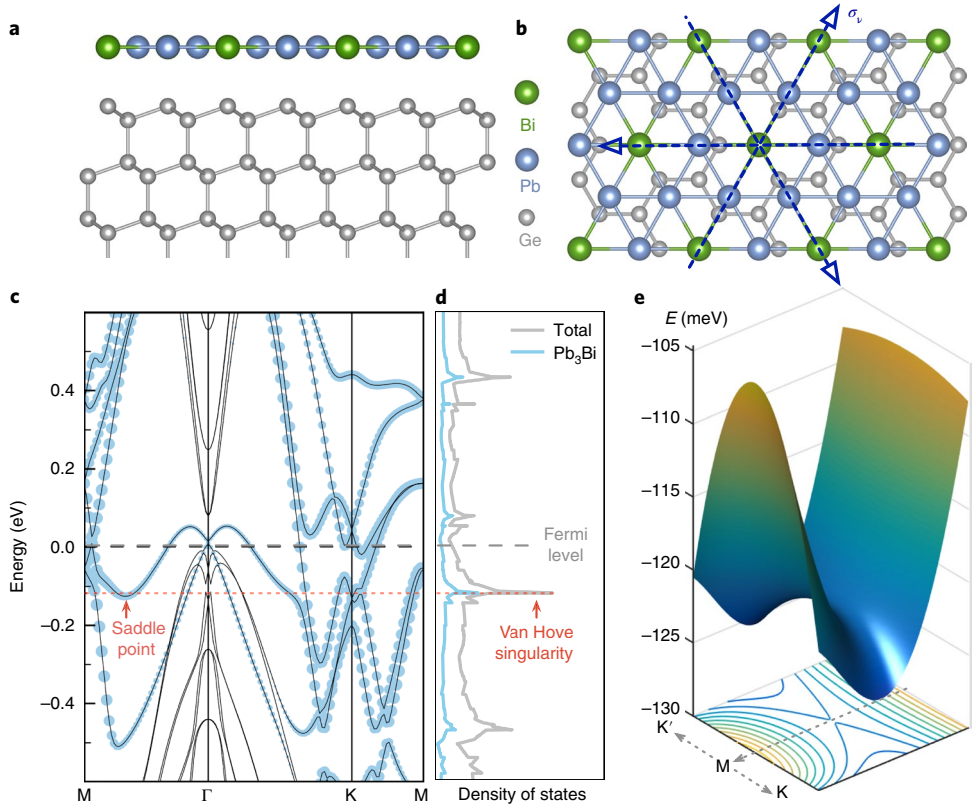

Fig. 1 | Crystal and electronic structures of Pb_3Bi/Ge(111). a,**b**, Side and top views of the crystal structure, with the dashed blue lines in **b** indicating the vertical mirror planes and σ_v denoting the reflection operator. **c**, Band structure of Pb_3Bi/Ge(111) with the sizes of the blue circles indicating the spectral weights contributed from the Pb_3Bi overlayer. The red arrow on the left marks the saddle point of the Rashba-split band. **d**, Total and partial density of states of the system, where a prominent type II van Hove singularity emerges at ~0.1 eV below the Fermi level. **e**, Enlarged band structure around a saddle point.

the hole band as an appealing platform for realizing chiral topological superconductivity in 2D systems.

The crystal structure of Pb_3Bi/Ge(111) is illustrated in Fig. 1a,b. The choice of this system was motivated by earlier observations that ultrathin Pb films on Si(111) or Ge(111) are superconducting[31,32], with indications of even higher superconducting transition temperatures following Bi alloying[33]. Furthermore, recent studies of related systems have shown giant Rashba spin–orbit coupling[34]. In the present study, we employ first-principles calculations within density functional theory to obtain the electronic structure of Pb_3Bi/Ge(111) (details are to be reported elsewhere). As shown in Fig. 1c–e, the band structure possesses two distinct features. First, the band around the Fermi level exhibits an extremely large Rashba splitting (larger than the pure Pb/Ge(111) system). The Rashba effect originates from the strong atomic spin–orbit coupling of Pb and Bi atoms, which are further subjected to an asymmetric potential induced by the substrate. Second, a saddle-like band structure is present, rooted in the Rashba band along the Γ–M direction (Fig. 1e). In contrast, the saddle-like band structure would be missing without spin–orbit coupling (Supplementary Fig. 2a). Because the present system simultaneously possesses three-fold rotational symmetry, mirror symmetry and time-reversal symmetry, there exist a total of six such symmetric saddle points within the Brillouin zone, leading to the logarithmically divergent type II van Hove singularity shown in Fig. 1d.

In systems that have a van Hove singularity and Fermi surface nesting, competing orders such as superconductivity, charge density wave, spin density wave and nematicity might emerge at low temperatures due to the subtle many-electron correlations[35]. It is vital to identify the dominant order under diverse physically realistic conditions. For example, an earlier RG analysis of doped graphene demonstrated chiral *d*-wave superconductivity as the leading competing order[36,37]. However, the exceedingly high van Hove singularity of 2.8 eV away from the Fermi level of pristine graphene hinders potential experimental observation of the predicted superconductivity. Most recently, this challenge has been overcome by using magic-angle twisted bilayer graphene, which exhibits superconductivity upon moderate gating to reach the van Hove singularity located close to the Fermi level[38]. In Pb_3Bi/Ge(111), the van Hove singularity is located ~0.1 eV below the Fermi level, as shown in Fig. 1d, and the calculated carrier density required to move the Fermi level to the van Hove singularity is $\sim 1.4\times10^{14}\,\mathrm{cm}^{-2}$, which is expected to be accessible via state-of-the-art ionic liquid gating[39]. Aside from the relative location of the van Hove singularity, its type II nature also favours superconductivity to be the leading instability, as demonstrated here.

A distinctive character of the present system is that the type II van Hove singularity originates from the Rashba-split band, which not only drastically increases the density of states that contributes to superconductivity[40], but, more importantly, endows the non-vanishing geometric phase to the relevant states[41]. Here, the geometric phase is characterized by spin-momentum locking, which possesses a clockwise form at the six saddle points (depicted in Supplementary Fig. 1) qualitatively extracted from the first-principles calculation results. In the vicinity of band crossing points, for example the Γ point in Fig. 1c, the Berry curvature field can be expressed as $\mathbf{\Omega}(\mathbf{r})=\kappa\mathbf{r}/2|\mathbf{r}|^3$, which defines a monopole with topological charge $\kappa=\pm1$ in the generalized 3D parameter space

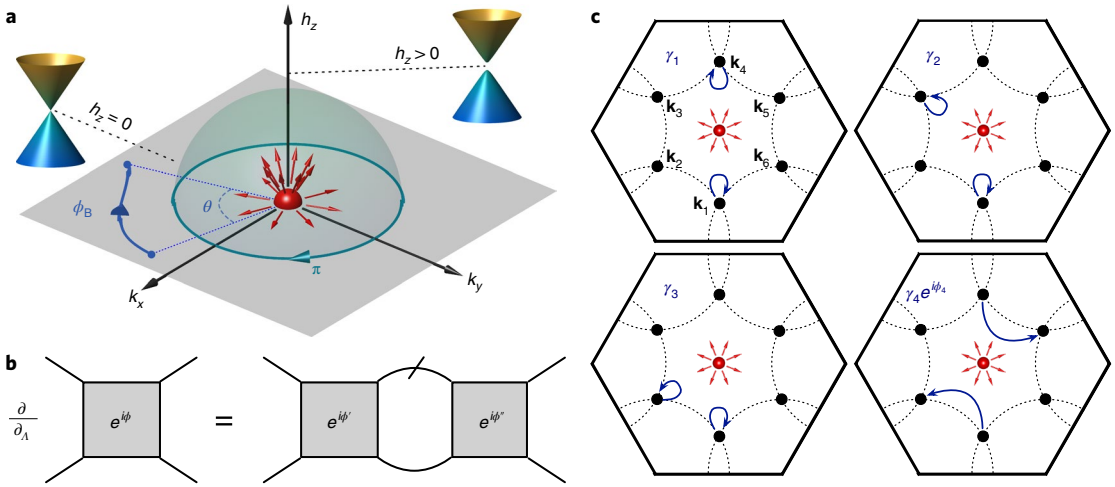

Fig. 2 | Geometric phase induced by a monopole. a, Schematic diagram of a monopole in the generalized 3D parameter space. The monopole (red sphere) is located at the centre of the momentum space, where the Rashba bands exhibit a Dirac point originating from band crossing. Within the projected 2D momentum space, an electron moving along a closed path (for example, the cyan circle) enclosing the monopole accumulates a phase π. In contrast, it acquires a phase ϕ_B along an unclosed trajectory (for example, the blue curve) determined by the geometric angle θ. **b**, Graphical representation of the one-loop RG flow equation decorated by geometric phases, where Λ denotes the ultraviolet cutoff. **c**, Graphical representations of four distinct scattering processes. Here, to succinctly demonstrate the essential ingredients involved in the present study, only a single monopole is depicted at the centre of the Brillouin zone, which generates Berry curvature fields in the parameter space, contributing a non-vanishing geometric phase to the fourth scattering channel. The remaining channels of $\gamma_{1,2,3}$ possess vanished geometric phases because of their local scattering nature.

spanned by $\mathbf{r}=(k_x, k_y, h_z)$ (ref. [42]). Here, $\mathbf{k}=(k_x, k_y)$ is the momentum vector, h_z is an auxiliary Zeeman field introduced for better visualization of the monopole (Supplementary Section I). As schematically depicted in Fig. 2a, a single electron moving in the projected 2D momentum space with $h_z=0$ accumulates a geometric phase ϕ_B. In the band representation, the presence of the monopole will further decorate the electron–electron interaction with a geometric phase as $V_{\mathbf{k}_1,\mathbf{k}_2';\mathbf{k}_2,\mathbf{k}_1}=\nu(\mathbf{q})\exp[i\phi_B(\mathbf{k}_1',\mathbf{k}_1)+i\phi_B(\mathbf{k}_2',\mathbf{k}_2)]$ (refs. [30,43,44]), where $\phi_B(\mathbf{k}',\mathbf{k})=\int_{\mathbf{k}}^{\mathbf{k}'}\mathcal{A}(\mathbf{k})\,\mathrm{d}\mathbf{k}$ is defined by the path integral of the vector potential $\mathcal{A}(\mathbf{k})$ in the momentum space. Going beyond these studies, here the central objective is to explore the delicate interplay between the geometric phase and electron correlation.

In treating this challenging problem, we note that conventional perturbation theory breaks down in the vicinity of a logarithmically divergent density of states, even in the weak coupling limit. Instead, the RG method provides an unbiased approach to deal with all the competing orders on an equal footing[45]. Because the low-energy physics depends mainly on the electron behaviours near the Fermi surface, we construct our model description within the patch approximation by considering only the electrons around the saddle point patches[29,36,46], which dominate the divergent density of states at the van Hove filling. In view of the fermionic anticommutation relation (Supplementary Section IV), there are a total of four inequivalent interacting channels between different patches, as depicted in Fig. 2c. Hence, the low-energy effective model of the present system can be formulated in the band representation as

$$\begin{aligned}\mathcal{L}=\sum_{n=1}^{6}\Big[&\psi_n^{\dagger}(\partial_\tau-\varepsilon_k+\mu)\psi_n-\frac{1}{2}(\gamma_1\psi_n^{\dagger}\psi_{\bar{n}}^{\dagger}\psi_{\bar{n}}\psi_n\\&+\gamma_2\psi_n^{\dagger}\psi_{\langle\bar{n}\rangle}^{\dagger}\psi_{\langle\bar{n}\rangle}\psi_n+\gamma_3\psi_n^{\dagger}\psi_{\langle n\rangle}^{\dagger}\psi_{\langle n\rangle}\psi_n)\\&+\frac{1}{2}(\gamma_4 e^{i\phi_4}\psi_{n+1}^{\dagger}\psi_{\bar{n}+1}^{\dagger}\psi_{\bar{n}}\psi_n+\mathrm{H.c.})\Big]\end{aligned}\qquad(1)$$

where the summation is over the patch index, ψ_n are the electron annihilation operators at patch n, $\bar{n}$ labels the patch with opposite momentum to n, and $\langle n\rangle$ denotes the nearest-neighbouring patches of n. Here, $\varepsilon_k\approx(\delta k_x)^2/2m_x-(\delta k_y)^2/2m_y$ is the energy dispersion of electrons expanded up to quadratic terms around each saddle point, with $\delta\mathbf{k}=\mathbf{k}-\mathbf{k}_n$, where $\mathbf{k}_n$ is the momentum of the corresponding saddle point as depicted in Fig. 2c. We note that the effects of spin-momentum locking are inherently imprinted into the saddle-like band dispersion and the geometric phase decorated electron–electron interaction (Supplementary Section II). The density of states around a given patch is derived as $g(\varepsilon)=2\nu_0\ln(4\Lambda/\varepsilon)$, where $\nu_0=\sqrt{m_xm_y}/4\pi^2$ and ε is the energy away from the van Hove singularity. The six saddle points are connected by three types of inequivalent nesting vectors $\mathbf{q}_n=\mathbf{k}_{n+1}-\mathbf{k}_1$ with $n=1, 2, 3$. The short-range interactions adopted here are expected to capture the essential low-energy physics because the metallic screening is sufficiently strong at the van Hove filling. We note that the effective model defined by equation (1) is conceptually generic, as its cornerstone is the very existence of the spin–orbit coupling-derived van Hove singularity near the Fermi level of the 2D system. More detailed discussions on the validity of this model as applied to the present prototypical system of Pb_3Bi are shown in Supplementary Section IV .

The essence of the RG analysis is to perform iterative integration over high-energy degrees of freedom, which yields a gradual evolution from the microscopic description to the final effective low-energy model. Generally, the coupling-constant space of a system depends on the energy cutoff separating the low- and high-energy regimes, indicating that a rescaling procedure that restores the energy cutoff should be invoked to ensure proper flows of the coupling constants. When specified to fermionic systems, the electron–electron interactions at finite frequencies and with momenta perpendicular to the Fermi surface are irrelevant under the RG transformation[47], indicating that the remaining or relevant coupling-constant space only depends on the static Fermi surface and is accordingly cutoff-independent. This unique feature justifies the validity of an unrescaled RG analysis in studying phase transitions, as typically employed in earlier studies[48,49]. Here, we derive the flows of the electron–electron interactions starting from the unrescaled functional RG differential equations, as detailed in Supplementary Section III. Specifically, the presence of non-vanishing geometric

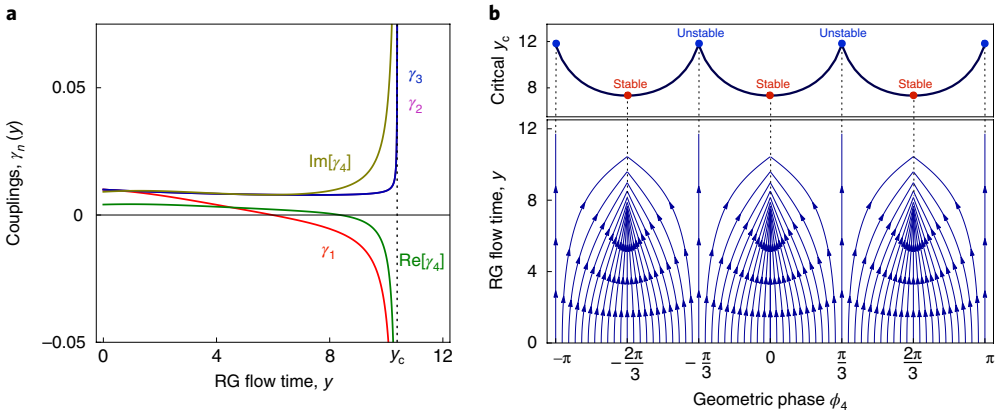

Fig. 3 | RG flows of the coupling strengths and geometric phase. a, Flow of the coupling strengths with respect to RG flow time y, where divergence occurs at y_c that indicates instability. The weak coupling regime is justified by taking the initial couplings as $\gamma_{1,2,3}=0.01$ and $\gamma_4=0.01e^{i\phi_4}$ with the specific geometric phase $\phi_4=\pi/3+0.1$ chosen for illustration. **b**, Flow of geometric phase ϕ_4 under RG transformation, where the red (blue) dots highlight the three stable (unstable) fixed points in the projected 1D phase space. The initial geometric phase varies from $-\pi$ to π while the other initial inputs are kept to be the same as in **a**.

phases decorates the one-loop RG flow equation, as shown graphically in Fig. 2b.

The RG flow equations are obtained by directly implementing the diagram depicted in Fig. 2b, where the dimensions of the coupling-constant space have been dramatically reduced within the patch approximation. Because all the involved interactions are marginal at the tree level, the one-loop diagram is able to capture the leading instabilities at low energies. For the convenience of identifying the critical temperature, we adopt $y=\ln(4\beta\Lambda)$ as the RG flow time, where $\beta=1/(k_BT)$, with k_B the Boltzmann constant, T the temperature and Λ the ultraviolet energy cutoff. As shown in Supplementary Section III, the building blocks for constructing RG flow equations are the various types of susceptibility, which vanish at $y=0$ and gradually increase with increasing y, indicating the relevant divergence is properly cured in a controllable manner. By redefining $\gamma_{1,2,3}\to\nu_0\gamma_{1,2,3}$ and $\gamma_4\to\nu_0\gamma_4e^{i\phi_4}$, we obtain a set of complex RG flow equations as

$$\begin{aligned}\frac{d\gamma_1}{dy}&=2(\eta-y)\gamma_1^2-8\gamma_2\gamma_3-4y|\gamma_4|^2\\ \frac{d\gamma_2}{dy}&=(\eta_1'-\eta_1-2)\gamma_2^2-4\gamma_1\gamma_3-2\gamma_3^2+\eta_1'|\gamma_4|^2\\ \frac{d\gamma_3}{dy}&=-4(\gamma_1\gamma_2+\gamma_2\gamma_3)+(\eta_1'-\eta_1)\gamma_3^2+\eta_1'|\gamma_4|^2\\ \frac{d\gamma_4}{dy}&=-4y\gamma_1\gamma_4+2y(\gamma_4^*)^2+2\eta_1'(\gamma_2+\gamma_3)\gamma_4\end{aligned}\tag{2}$$

where γ_4^* denotes the complex conjugate of γ_4. The coefficients η, η_1 and η_1' depend on the mass ratio m_x/m_y, characterizing the degrees of the Fermi surface nesting between different patches. For the present prototypical system, $\eta\approx1$, $\eta_1\approx1.65$ and $\eta_1'\approx1.79$, obtained by fitting the first-principles results. A close inspection of the above differential equations shows that $\gamma_2=\gamma_3$ manifests as a special solution. By integrating equation (2) with a set of initial inputs, we obtain the flows of the couplings as functions of y. As shown in Fig. 3a, the couplings diverge at y_c, indicating that the system is unstable at a critical temperature of $T_c\sim4\Lambda e^{-y_c}$. We note that the above RG flow equations are obtained by exploiting the unrescaled functional RG approach. A detailed rescaling treatment is presented in Supplementary Section V, with the temperature renormalized under the RG transformation[50]. Such a crosschecking shows that temperature renormalization only slightly suppresses T_c, but does not alter the divergent behaviours of the couplings and the central findings of the present study.

The renormalized geometric phase ϕ_4 as a function of y is displayed in Fig. 3b, demonstrating that the geometric phase and electron correlation are intimately coupled, which in turn gives rise to two constructive consequences. First, the geometric phase exhibits non-trivial evolution under the RG transformation and flows to three stable fixed points at $\pm2\pi/3$ and 0 in the projected 1D phase space. In the following, we will demonstrate that the non-trivial geometric phases at the stable fixed points will convert the leading order of superconductivity induced by the electron correlations into respective chiral $(p_x\pm ip_y)$-wave and f-wave superconducting states. Second, as shown in the upper panel of Fig. 3b, the magnitude of y_c depends on the initial value of ϕ_4 and possesses a degenerate minimum at the stable fixed points, indicating that the corresponding superconductivity can be substantially enhanced. As a secondary observation, there are also three unstable fixed points at $\pm\pi/3$ and π with a degenerate maximum of y_c.

To identify the dominant instability of the system, we need to evaluate the susceptibilities of various competing orders, which are defined as

$$\chi_{\alpha\beta}=\frac{\partial^2\ln(\mathcal{Z})}{\partial\rho_\alpha\partial\rho_\beta}\Big|_{\rho=0}\tag{3}$$

where $\mathcal{Z}$ is the partition function of the system and ρ denotes small external fields. For example, in the Bardeen–Cooper–Schrieffer (BCS) channel, ρ represents the superconducting order parameter (Supplementary Section VI). The RG flow equation of the order parameter $\boldsymbol{\Delta}$ in the zero-momentum BCS channel is governed by $\partial_y\boldsymbol{\Delta}=-y\Gamma_0\boldsymbol{\Delta}$ (Supplementary Section VI), where Γ_0 denotes the interaction matrix obtained as

$$\Gamma_0=\begin{bmatrix}\mathcal{M}&-\mathcal{M}\\-\mathcal{M}&\mathcal{M}\end{bmatrix},\quad\mathcal{M}=\begin{pmatrix}\gamma_1&\gamma_4&-\gamma_4^*\\\gamma_4^*&\gamma_1&\gamma_4\\-\gamma_4&\gamma_4^*&\gamma_1\end{pmatrix}\tag{4}$$

where $\gamma_{1,4}$ are obtained by solving equation (2). As a concrete and important example, we focus on the stable fixed point with the

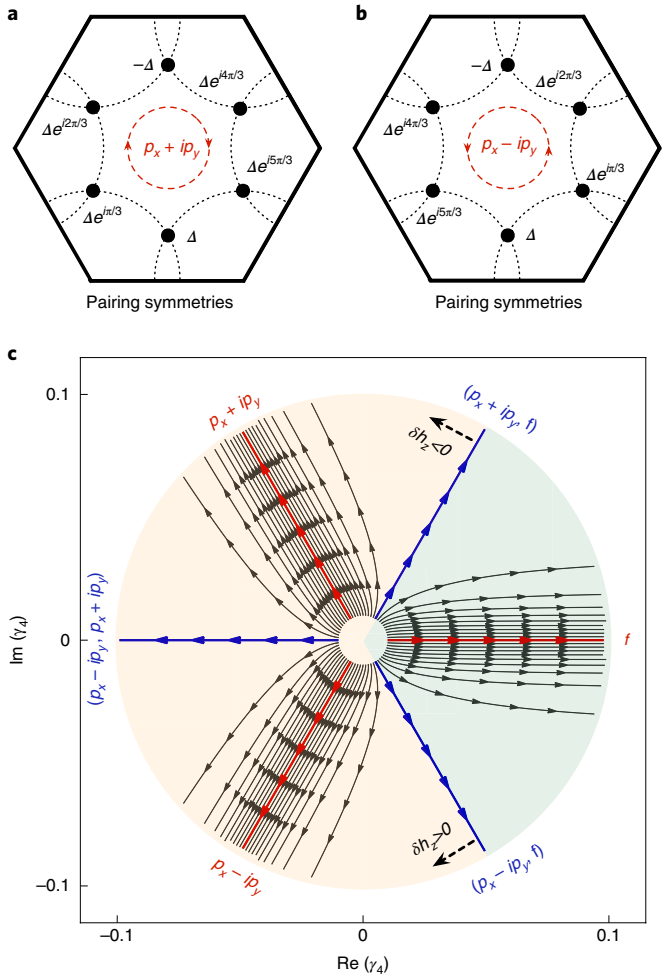

Fig. 4 | Phase diagram of the superconducting states. a,**b**, Superconducting order parameter with the pairing symmetry of $p_x + ip_y$ (**a**) or $p_x - ip_y$ (**b**), possessing 2π or -2π phase when winding around the Fermi surface, respectively. **c**, Phase diagram spanned by γ_4. Here, the solid lines with arrows represent the flows of γ_4 under RG transformation, and the red (blue) lines denote the stable (unstable) fixed points. The geometric phases within the three distinct ranges defined by $\phi_4 \in (-\pi/3, \pi/3)$, $(\pi/3, \pi)$ and $(-\pi/3, -\pi)$ are renormalized to the three stable fixed points characterized by $\phi_4 = 0, \pm 2\pi/3$, respectively. The dashed arrows indicate that the three unstable fixed points can be driven into stable fixed points by Zeeman fluctuations.

renormalized geometric phase $\phi_4 = 2\pi/3$, where $\gamma_4 = |\gamma_4| e^{i2\pi/3}$. The non-trivial eigenvectors of Γ_0 are obtained as

$$\begin{aligned}
\Delta_a &= \frac{\Delta}{\sqrt{6}}(1, e^{i\pi/3}, e^{i2\pi/3}, -1, e^{i4\pi/3}, e^{i5\pi/3}) \\
\Delta_{b_1} &= \frac{\Delta}{2}(e^{i\pi/3}, e^{-i\pi/3}, 0, e^{-i2\pi/3}, e^{i2\pi/3}, 0) \\
\Delta_{b_2} &= \frac{\Delta}{2}(e^{-i\pi/3}, 0, e^{-i2\pi/3}, e^{i2\pi/3}, 0, e^{i\pi/3})
\end{aligned} \tag{5}$$

with the corresponding eigenvalues of $\varepsilon_a = 2(\gamma_1 - 2|\gamma_4|)$ and $\varepsilon_{b_{1,2}} = 2(\gamma_1 + |\gamma_4|)$. Here $\mathbf{\Delta}_a$ characterizes the chiral $(p_x + ip_y)$-wave superconducting state, which possesses a 2π phase upon winding around the Fermi surface, as shown in Fig. 4a, while $\Delta_{b_{1,2}}$ are degenerate and non-orthogonal, stemming from the mixing between the

Table 1 | Competing orders

	Zero momentum	Finite momenta
BCS	$\alpha_a = 2y_c(\Gamma_1 - 2\lvert\Gamma_4\rvert)$	$\alpha(\mathbf{q}_1) = \eta_1\Gamma_2$
	$\alpha_b = 2y_c(\Gamma_1 + \lvert\Gamma_4\rvert)$	$\alpha(\mathbf{q}_2) = \eta_1\Gamma_3$
Charge density wave	$\beta_s = 2\Gamma_1 + 4(\Gamma_2 + \Gamma_3)$	$\beta_\pm(\mathbf{q}_2) = \eta_1'(-\Gamma_3 \pm \lvert\Gamma_4\rvert)$
	$\beta_p = -2\Gamma_1 - 2(\Gamma_2 - \Gamma_3)$	$\beta_\pm(\mathbf{q}_3) = \eta_1'(-\Gamma_2 \pm \lvert\Gamma_4\rvert)$
	$\beta_d = 2\Gamma_1 - 2(\Gamma_2 + \Gamma_3)$	$\beta(\mathbf{q}_4) = -2\eta\Gamma_1$
	$\beta_f = -2\Gamma_1 + 4(\Gamma_2 - \Gamma_3)$	

Divergent coefficients for different channels of competing orders, with $\phi_4 = 2\pi/3$ for specific illustration.

$(p_x - ip_y)$-wave and f-wave superconducting states (Supplementary Section VI). Using the eigenvector basis, the RG flow equation of the order parameter reduces to

$$\partial_y \ln \Delta_n = -\varepsilon_n y \tag{6}$$

where n denotes a and $b_{1,2}$. Near the instability threshold y_c, the interactions scale as $\gamma_i = \Gamma_i/(y_c - y)$. By substituting the scaling forms of $\gamma_{1,4}$ into equation (6), we find the superconducting susceptibilities to diverge as

$$\chi_n \sim \Delta_n(y)/\Delta_n(0) \sim (y_c - y)^{\alpha_n} \tag{7}$$

where $\alpha_a = 2y_c(\Gamma_1 - 2|\Gamma_4|)$ and $\alpha_b = 2y_c(\Gamma_1 + |\Gamma_4|)$. Here Γ_i can be obtained by substituting the scaling forms of γ_i into equation (2). From Fig. 3a and also more generally, we obtain Γ_1 as negative definite in the parameter space spanned by η_1 and η_1'. Because the most negative coefficient of α determines the leading instability, the situation at focus highly prefers the chiral $(p_x + ip_y)$-wave superconducting state rather than the degenerate superconducting states characterized by $\Delta_{b_{1,2}}$.

Similarly, we can calculate the susceptibilities of the finite-momentum BCS channels and charge density wave channels (Supplementary Section VI), with the corresponding divergent coefficients as listed in Table 1. In the weak interaction regime, the RG critical time $y_c \gg |\Gamma|$, indicating that zero-momentum superconductivity dominates over other competing orders (Table 1). Moreover, by investigating the various types of susceptibility for the remaining stable and unstable fixed points, we can construct a phase diagram of the topological quantum states as shown in Fig. 4c. The stable fixed points with renormalized geometric phase $\phi_4 = \pm 2\pi/3$ and 0 prefer the non-degenerate $(p_x \pm ip_y)$-wave and f-wave superconducting states, respectively. In contrast, each of the unstable fixed points prefers doubly degenerate pairing states defined by the neighbouring stable fixed points (Fig. 4c). Here, a subtle point to note is that the superconducting states presented in Fig. 4c cover all possible zero-momentum pairings within the context of the present model study. In particular, the momentum-derived chiral p-wave or f-wave superconducting state is concurrently characterized by spin singlet and triplet mixed pairing in our non-centrosymmetric system[51] (Supplementary Section VI).

Based on the phase diagram depicted in Fig. 4c, we propose that hole-doped Pb_3Bi/Ge(111) can serve as an appealing platform for realizing a 2D chiral topological superconductor due to the subtle interplay between the geometric phase and electron correlation. Depending on the pairing nature of the superconducting system, there are two conceptually different approaches to realize topological superconductors. First, if the phonon or other boson mediated electron–electron attraction overwhelms the Coulomb repulsion, the system already possesses a net attractive interaction between the

electrons without the assistance of the geometric phase. In addition, as detailed in Supplementary Section VII, only the monopole at the Γ point contributes a finite geometric phase of $\pm\pi/3$ to the interacting channel γ_4, driving the system from the unstable fixed point with $\phi_4=\pi$ to the stable fixed points with $\phi_4=\pm 2\pi/3$. Consequently, we reach the chiral $(p_x \pm ip_y)$-wave superconducting states. Moreover, the corresponding superconductivity has also been substantially enhanced. Second, if the Coulomb repulsion overwhelms the boson-mediated attraction, the geometric phase of $\pm\pi/3$ provided by the monopole at the Γ point can drive the system from the stable fixed point with $\phi_4=0$ to the unstable fixed points with $\phi_4=\pm\pi/3$. Even in such situations, by applying a physically realistic Zeeman fluctuation of δh_z to move the monopole out of the 2D momentum space (Supplementary Section VII), the system can again be renormalized and stabilized to reach the chiral $(p_x \pm ip_y)$-wave superconducting states, as illustrated in Fig. 4c. Therefore, robust topological superconductivity is highly preferred in such superconducting materials with relatively generic pairing mechanisms.

Given the generic nature of the microscopic formalism developed in this study, it is expected that other types of quasi-2D superconducting overlayer on proper substrates could also harbour topological superconductivity, as long as those systems possess proper spin–orbit coupling. Candidate systems may include Te-doped FeSe or Te-doped $NbSe_2$ superconducting overlayers. Indications of the topologically non-trivial nature of the former in the thin-film or bulk form have been reported in recent experiments[26–28]. For the latter, it would also be intriguing to see how Ising superconductivity and topological superconductivity might entangle[52]. Overall, the insights gained in this study will prove to be instrumental in searching for new types of 2D topological superconductor that may exhibit emergent physical phenomena; these systems are also inherently superior to existing platforms for detecting and braiding Majorana fermions.

Online content

Any methods, additional references, Nature Research reporting summaries, source data, statements of code and data availability and associated accession codes are available at https://doi.org/10.1038/s41567-019-0517-5.

Data availability

The data that support the plots within this paper and other findings of this study are available from the corresponding author on request.

Received: 26 May 2018; Accepted: 2 April 2019;
Published online: 6 May 2019

References

1. Berry, M. V. Quantal phase factors accompanying adiabatic changes. *Proc. R. Soc. Lond. A* **392**, 45–57 (1984).
2. Zak, J. Berry's phase for energy bands in solids. *Phys. Rev. Lett.* **62**, 2747–2750 (1989).
3. Xiao, D., Chang, M.-C. & Niu, Q. Berry phase effects on electronic properties. *Rev. Mod. Phys.* **82**, 1959–2007 (2010).
4. Qi, X.-L., Hughes, T. L. & Zhang, S.-C. Topological field theory of time-reversal invariant insulators. *Phys. Rev. B* **78**, 195424 (2008).
5. Essin, A. M., Moore, J. E. & Vanderbilt, D. Magnetoelectric polarizability and axion electrodynamics in crystalline insulators. *Phys. Rev. Lett.* **102**, 146805 (2009).
6. Hughes, T. L., Prodan, E. & Bernevig, B. A. Inversion-symmetric topological insulators. *Phys. Rev. B* **83**, 245132 (2011).
7. Thouless, D. J., Kohmoto, M., Nightingale, M. P. & den Nijs, M. Quantized Hall conductance in a two-dimensional periodic potential. *Phys. Rev. Lett.* **49**, 405–408 (1982).
8. Murakami, S. & Nagaosa, N. Berry phase in magnetic superconductors. *Phys. Rev. Lett.* **90**, 057002 (2003).
9. Li, Y. & Haldane, F. D. M. Topological nodal cooper pairing in doped Weyl metals. *Phys. Rev. Lett.* **120**, 067003 (2018).
10. Sato, M. Topological properties of spin-triplet superconductors and Fermi surface topology in the normal state. *Phys. Rev. B* **79**, 214526 (2009).
11. Qi, X.-L., Hughes, T. L. & Zhang, S.-C. Topological invariants for the Fermi surface of a time-reversal-invariant superconductor. *Phys. Rev. B* **81**, 134508 (2010).
12. Sato, M. Topological odd-parity superconductors. *Phys. Rev. B* **81**, 220504 (2010).
13. Fu, L. & Berg, E. Odd-parity topological superconductors: theory and application to $Cu_xBi_2Se_3$. *Phys. Rev. Lett.* **105**, 097001 (2010).
14. Qi, X.-L. & Zhang, S.-C. Topological insulators and superconductors. *Rev. Mod. Phys.* **83**, 1057–1110 (2011).
15. Alicea, J. New directions in the pursuit of Majorana fermions in solid state systems. *Rep. Prog. Phys.* **75**, 076501 (2012).
16. Read, N. & Green, D. Paired states of fermions in two dimensions with breaking of parity and time-reversal symmetries and the fractional quantum Hall effect. *Phys. Rev. B* **61**, 10267–10297 (2000).
17. Ivanov, D. A. Non-abelian statistics of half-quantum vortices in *p*-wave superconductors. *Phys. Rev. Lett.* **86**, 268–271 (2001).
18. Nayak, C., Simon, S. H., Stern, A., Freedman, M. & Das Sarma, S. Non-abelian anyons and topological quantum computation. *Rev. Mod. Phys.* **80**, 1083–1159 (2008).
19. Fu, L. & Kane, C. L. Superconducting proximity effect and Majorana fermions at the surface of a topological insulator. *Phys. Rev. Lett.* **100**, 096407 (2008).
20. Sau, J. D., Lutchyn, R. M., Tewari, S. & Das Sarma, S. Generic new platform for topological quantum computation using semiconductor heterostructures. *Phys. Rev. Lett.* **104**, 040502 (2010).
21. Wang, Z. et al. Topological nature of the $FeSe_{0.5}Te_{0.5}$ superconductor. *Phys. Rev. B* **92**, 115119 (2015).
22. Sasaki, S. et al. Topological superconductivity in $Cu_xBi_2Se_3$. *Phys. Rev. Lett.* **107**, 217001 (2011).
23. Wang, M.-X. et al. The coexistence of superconductivity and topological order in the Bi_2Se_3 thin films. *Science* **336**, 52–55 (2012).
24. Matano, K., Kriener, M., Segawa, K., Ando, Y. & Zheng, G.-Q. Spin-rotation symmetry breaking in the superconducting state of $Cu_xBi_2Se_3$. *Nat. Phys.* **12**, 852–854 (2016).
25. Sun, H.-H. et al. Majorana zero mode detected with spin selective Andreev reflection in the vortex of a topological superconductor. *Phys. Rev. Lett.* **116**, 257003 (2016).
26. Shi, X. et al. $FeTe_{1-x}Se_x$ monolayer films: towards the realization of high-temperature connate topological superconductivity. *Sci. Bull.* **62**, 503–507 (2017).
27. Zhang, P. et al. Observation of topological superconductivity on the surface of an iron-based superconductor. *Science* **360**, 182–186 (2018).
28. Wang, D. et al. Evidence for Majorana bound states in an iron-based superconductor. *Science* **362**, 333–335 (2018).
29. Yao, H. & Yang, F. Topological odd-parity superconductivity at type-II two-dimensional van Hove singularities. *Phys. Rev. B* **92**, 035132 (2015).
30. Shi, J. & Niu, Q. Attractive electron–electron interaction induced by geometric phase in a Bloch band. Preprint at https://arxiv.org/abs/cond-mat/0601531 (2006).
31. Qin, S., Kim, J., Niu, Q. & Shih, C.-K. Superconductivity at the two-dimensional limit. *Science* **324**, 1314–1317 (2009).
32. Zhang, T. et al. Superconductivity in one-atomic-layer metal films grown on Si(111). *Nat. Phys.* **6**, 104–108 (2010).
33. Özer, M. M., Jia, Y., Zhang, Z., Thompson, J. R. & Weitering, H. H. Tuning the quantum stability and superconductivity of ultrathin metal alloys. *Science* **316**, 1594–1597 (2007).
34. Matetskiy, A. V. et al. Two-dimensional superconductor with a giant Rashba effect: one-atom-layer Tl–Pb compound on Si(111). *Phys. Rev. Lett.* **115**, 147003 (2015).
35. Hur, K. L. & Rice, T. M. Superconductivity close to the Mott state: from condensed-matter systems to superfluidity in optical lattices. *Ann. Phys.* **324**, 1452–1515 (2009).
36. Nandkishore, R., Levitov, L. S. & Chubukov, A. V. Chiral superconductivity from repulsive interactions in doped graphene. *Nat. Phys.* **8**, 158–163 (2012).
37. Nandkishore, R., Thomale, R. & Chubukov, A. V. Superconductivity from weak repulsion in hexagonal lattice systems. *Phys. Rev. B* **89**, 144501 (2014).
38. Cao, Y. et al. Unconventional superconductivity in magic-angle graphene superlattices. *Nature* **556**, 43–50 (2018).
39. Ye, J. T. et al. Liquid-gated interface superconductivity on an atomically flat film. *Nat. Mater.* **9**, 125–128 (2009).
40. Cappelluti, E., Grimaldi, C. & Marsiglio, F. Topological change of the Fermi surface in low-density Rashba gases: application to superconductivity. *Phys. Rev. Lett.* **98**, 167002 (2007).
41. Murakawa, H. et al. Detection of Berry's phase in a bulk Rashba semiconductor. *Science* **342**, 1490–1493 (2013).
42. Fang, Z. et al. The anomalous Hall effect and magnetic monopoles in momentum space. *Science* **302**, 92–95 (2003).

43. Zhang, C., Tewari, S., Lutchyn, R. M. & Das Sarma, S. p_x+ip_y superfluid from *s*-wave interactions of fermionic cold atoms. *Phys. Rev. Lett.* **101**, 160401 (2008).
44. Mao, L., Shi, J., Niu, Q. & Zhang, C. Superconducting phase with a chiral *f*-wave pairing symmetry and Majorana fermions induced in a hole-doped semiconductor. *Phys. Rev. Lett.* **106**, 157003 (2011).
45. Shankar, R. Renormalization-group approach to interacting fermions. *Rev. Mod. Phys.* **66**, 129–192 (1994).
46. Furukawa, N., Rice, T. M. & Salmhofer, M. Truncation of a two-dimensional Fermi surface due to quasiparticle gap formation at the saddle points. *Phys. Rev. Lett.* **81**, 3195–3198 (1998).
47. Metzner, W., Salmhofer, M., Honerkamp, C., Meden, V. & Schönhammer, K. Functional renormalization group approach to correlated fermion systems. *Rev. Mod. Phys.* **84**, 299–352 (2012).
48. Halboth, C. J. & Metzner, W. Renormalization-group analysis of the two-dimensional Hubbard model. *Phys. Rev. B* **61**, 7364–7377 (2000).
49. Kampf, A. P. & Katanin, A. A. Competing phases in the extended *U*–*V*–*J* Hubbard model near the van Hove fillings. *Phys. Rev. B* **67**, 125104 (2003).
50. Millis, A. J. Effect of a nonzero temperature on quantum critical points in itinerant fermion systems. *Phys. Rev. B* **48**, 7183–7196 (1993).
51. Gor'kov, L. P. & Rashba, E. I. Superconducting 2D system with lifted spin degeneracy: mixed singlet–triplet state. *Phys. Rev. Lett.* **87**, 037004 (2001).
52. Lu, J. M. et al. Evidence for two-dimensional Ising superconductivity in gated MoS_2. *Science* **350**, 1353–1357 (2015).

Acknowledgements

This work was supported by the National Natural Science Foundation of China (grants nos 11634011 and 61434002), the National Key R&D Program of China (grant no. 2017YFA0303500), Anhui Initiative in Quantum Information Technologies (grant no. AHY170000) and the Strategic Priority Research Program of Chinese Academy of Sciences (grant no. XDB30000000).

Author contributions

Z.Y.Z. initiated and directed the project. W.Q. carried out the theoretical studies and analyses. L.Q.L. performed the first-principles calculations. W.Q. wrote the manuscript and Z.Y.Z. edited the manuscript.

Competing interests

The authors declare no competing interests.

Additional information

Supplementary information is available for this paper at https://doi.org/10.1038/s41567-019-0517-5.

Reprints and permissions information is available at www.nature.com/reprints.

Correspondence and requests for materials should be addressed to Z.Y.Z.

Publisher's note: Springer Nature remains neutral with regard to jurisdictional claims in published maps and institutional affiliations.